3D multi-valued traveltime and amplitude maps II

Lan Wang and Norman Bleistein
Center for Wave Phenomena

ABSTRACT

Accurate and efficient forward modeling is a key part in 3D prestack migration/inversion. In an earlier paper, the authors described a ray-theoretical modeling method that uses physical model smoothing, dynamic ray tracing and wavefront construction. All the quantities in the Bleistein-Cohen inversion formula can be determined by that method.

In this report, we provide some sample implementations of this method. The accuracy of the smoothing procedure is tested by application on a horizontal-interface model with strong velocity contrast where we show that the amplitude and traveltime adequately match an analytical solution of the discontinuous model problem in the forward propagating direction. We also address the problem of multi-pathing and caustics and show that the method produces the amplitude and phase on all arrivals at depth. The final example is taken from a section of the SEG/EAGE saltdome model. Here, the method properly characterizes the sparse penetration of rays into the saltdome, itself, as well as the transmission below.

Key words: amplitude, dynamic ray tracing, wavefront construction, multi-pathing, caustics

Introduction

Kirchhoff migration is generally accepted to be the most efficient method of imaging 2D, 2.5D and 3D prestack seismic reflection data. A key part of this method is traveltime computation. Several studies (Geoltrain & Brac, 1993; Albertin *et al.*, 1996; Audebert *et al.*, 1997) have shown that the use of the traveltimes associated with the most energetic arrivals in Kirchhoff migration instead of the wavefield of the first arrival traveltimes will significantly improve the image in complex structure, where the first arrivals only carry a fraction of the total energy of the source. Migration and inversion methods that process first arrivals, only, disperse the energy of later arrivals of the data, effectively treating it as noise. The portion of a wave front carried on rays that pass through caustics are known to exhibit a phase shift that is characterized by a phase shift index—the KMAH index, named for Keller, Maslov, Arnol'd and Hörmander. It is necessary to include this phase shift in the various approaches of amplitude-preserving Kirchhoff depth migration/inversions, such as Bleistein-Cohen inversion (Bleistein *et al.*, 1987; Bleistein *et al.*, 1996). In these methods, the weighted diffraction stack produces the angular dependent reflection coefficients, in addition to the correct location of the structural interfaces. The inversion process depends on the computations of traveltimes, ray amplitudes and Beylkin determinant, which characterizes the source and receiver configuration. Even in Kirchhoff migration stacking, phase shifts that are not taken into account will transform impulse-like source signatures into doublets on output, causing uncertainty in the location of reflection events.

Accurate and efficient forward modeling is one of the bottlenecks in Kirchhoff depth imaging and inversion. In (Wang & Bleistein, 1998), we described a ray-theoretical forward modeling method using dynamic ray tracing and wavefront construction. The ray-tracing component provides accurate multi-valued traveltimes, ray amplitudes, and phase-shifts. Červený and de Castro (1993) pointed out that the Beylkin determinant in the inversion formula can also be determined by dynamic ray tracing. The wavefront construction approach makes the algo-

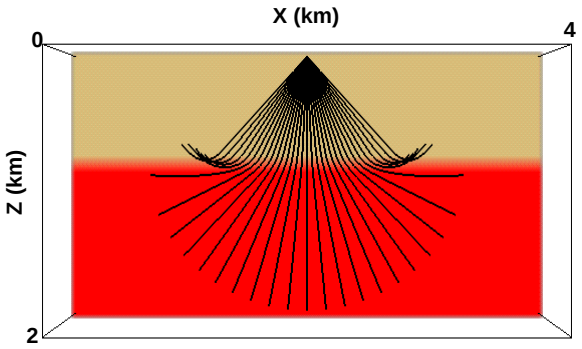

Figure 1. Rays in horizontal-interface model of strong velocity variation. The velocities are 2 km/s in the upper layer and 4 km/s in the lower layer.

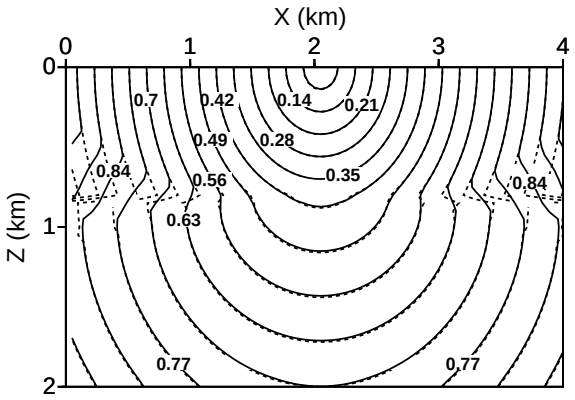

Figure 2. Traveltime comparison for horizontal-interface model. The solid curves depict the in-plane wavefronts, or isochrons, computed from the smoothed model; the dashed curves depict the wavefronts for the analytic solutions.

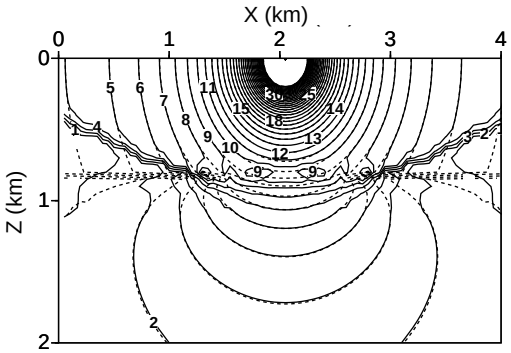

Figure 3. Amplitude comparison for horizontal-interface model. The solid curves depict the computed level curves of amplitude from the smoothed model and the dashed curves depict the level curves for the analytic solutions, with the transmission coefficient set equal to 1.

rithm more efficient than traditional shooting methods and provides better ray coverage. The technique is suitable for 3D models with isotropic, smoothly varying velocities.

There are faster ray tracers available, such as Meng and Bleistein (1997), in which the earth model is decomposed into tetrahedra with linearized slowness in each tetrahedral cell. Methods such as this one do not provide sufficient smoothness of the velocity model for accurate amplitude computation. The method we propose here provides a reasonable compromise between speed and accuracy of the wavefield needed for inversion processing.

We describe three examples of dynamic ray tracing. Each example is indicative of a situation that is common in applications. As discussed in Wang and Bleistein (1998), the ray tracing technique is carried out on smoothed gridded velocity models.

As a first test of our method, we construct the wavefield for a model consisting of a single horizontal-interface, with a strong velocity contrast. We compare the numerical output for the smoothed model with the analytic solutions for the underlying discontinuous model. The comparison show satisfactory accuracy of the transmitted amplitude, as well as traveltime. This is the direction of most interest to us for application to Kirchhoff inversion. In the comparison, the transmission coefficient in the analytical solution was set equal to unity, since our numerical method does not yet account for transmission coefficients. That is a subject for future work.

We also show results of applying our method to a model consisting of a low velocity lens inclusion in an otherwise vertically monotonic velocity distribution. This earth model produces rays that exhibit multipathing and different kinds of caustics. Here, the first arrivals at depth are not always the most energetic arrivals. The separation of the various arrivals by the computer code is demonstrated.

The last example is based on a section of the SEG/EAGE saltdome model. The output demonstrates the ability of this method to treat the extreme contrasts across the saltdome interface and into the subsalt region, below.

Example I — horizontal-interface model

The preconditioning (smoothing) of the velocity model needed in this method leads to a question of the accuracy of the traveltimes and amplitudes transmitted through a sharp interface. This first simple example tests that accuracy.

Inversion procedures actually require a smooth background velocity in the region of the interface being

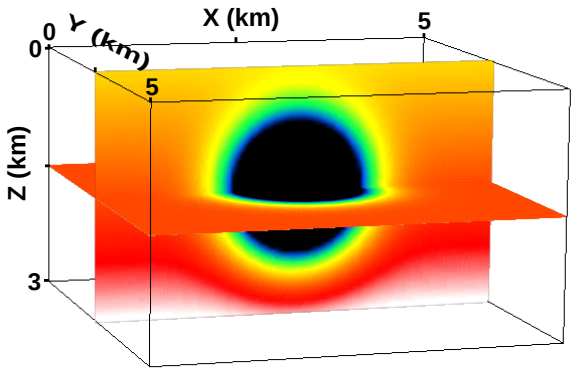

Figure 4. Lens model. A spherical low velocity lens is wedged into high velocity surroundings.

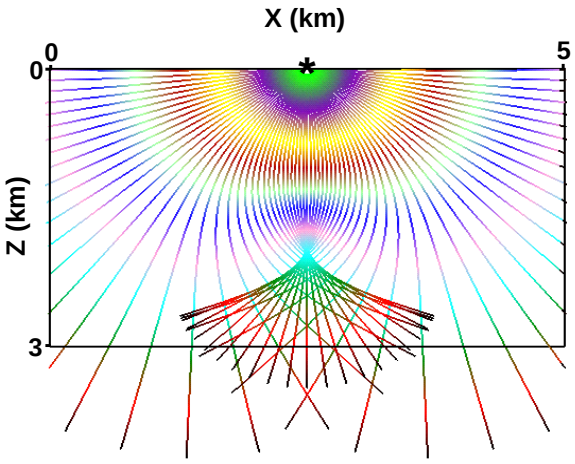

Figure 5. Rays in lens model. The color represents the traveltime along the ray.

constructed. The inversion then delineates the discontinuous surface where the background model was continuous. This ray tracing method requires a velocity field that has continuous first and second derivatives everywhere. Thus, as the processing moves deeper into the subsurface, the earth model used for ray tracing and the earth model determined by inversion in the overburden disagree. Nonetheless, inversion requires that the transmitted wavefield remain reasonably close to the wavefield of a discontinuous overburden. The example chosen here provides a first test of the agreement of the transmitted wavefield produced numerically by using a smoothed velocity model and an analytical wavefield produced from the underlying discontinuous model.

The velocity model (see Fig 1) consists of two constant layers, separated by a horizontal interface. The velocities are 2 km/s in the upper layer, and 4 km/s in the lower layer. The interface between the two layers is smoothed with a Gaussian-tapered box weighting function, and is replaced by a smooth transition zone. This smoothing is actually applied to slowness—inverse velocity. It has been our experience that this provides the most accurate traveltimes and amplitudes. Figure 1 shows rays traced in the smoothed velocity model. Rays propagate across the interface zone smoothly, with post-critical rays smoothly refracted upward after entering the smoothed transition zone. The rays with near critical take-off angles refracted into the transition zone and formed a transition wavefield similar to a head wave.

Figure 2 shows the traveltime comparison. The dashed curves are the analytic in-plane wavefronts, and the solid curves are computed results. In this example, the first-arrivals program option was used. The only significant difference between these two solution is in the post-critical region near the interface. The pseudo-head-waves connect the direct waves in the two layers. When the most energetic or shortest ray-path ray option is chosen, the wavefronts will consist of direct rays only, and exclude the pseudo-head-waves. However, this difference is less important to us; it is the wavefield in the transmitted zone that we are going to use for the migration/inversion, not the wavefield in the post-critical region. The transmitted wave traveltimes of the numerical and analytical solutions are shown to be in good agreement in this figure.

Figure 3 shows the amplitude comparison, with the dashed curves showing the level curves of amplitude for analytic solution, and the solid curves used for the computed results. Our numerical code does not yet include transmission coefficients, so we did not include that factor in our analytical amplitude calculation. Thus, we are only checking the agreement of the ray Jacobians for the smooth and the discontinuous velocity models. Once again, the code is less accurate at post-critical, near the interface. The head wave amplitude is much lower than the direct wave amplitude, leading to the dense placement of level curves through the region of transition from direct wave to head wave. However, the numerical and analytical amplitudes are seen to agree with each other very well elsewhere, including the transmitted region. Again, we remind the reader that this is the region in which we are going to use the wavefield for inversion.

Figures 2 and 3 indicate that even in the presence of a sharply discontinuous interface in the original velocity model, our ray tracing method provides accurate transmitted traveltime and amplitude (up to a transmission coefficient).

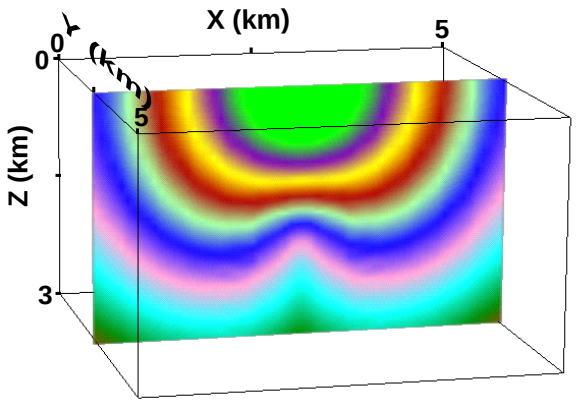

Figure 6. Traveltime of first arrivals in lens model.

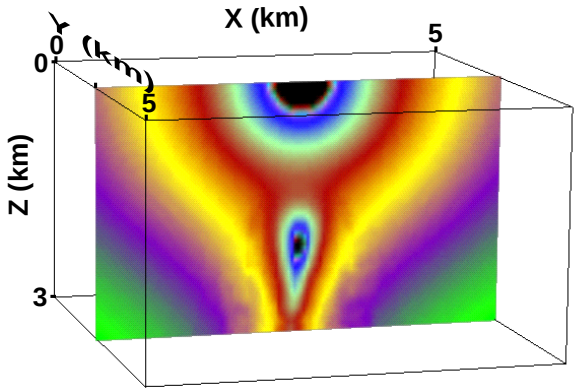

Figure 7. Amplitude of first arrivals in lens model.

Example II — lens model

This example demonstrates the ability of our code to deal with multi-pathing and caustics. Multiple arrivals are a common phenomenon in inhomogeneous media. One would expect a focusing of energy in the low velocity region and a defocusing in the surrounding high velocity region. In the presence of multi-pathing, the latter arrivals may carry more energy, and the amplitude coefficients exhibit phase shifts arising from passage through caustics. Therefore, it is important for the forward modeling algorithm to have the ability to find all the possible arrivals and amplitude coefficients. We remark that the current code only deals with the more standard caustics of isotropic media. More exotic caustics produced by anisotropy do not lend themselves to adjustment via a simple KMAH index (de Hoop & Brandsberg-Dahl, 1998).

Figure 4 shows the velocity distribution of a lens model. A spherical-shape low velocity lens is included in

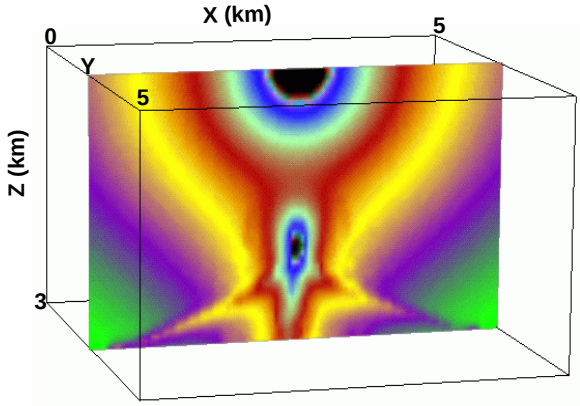

Figure 8. Amplitude of most energetic arrivals in lens model.

an otherwise high velocity zone, with velocity monotonically increasing with depth. Figure 5 shows some in-plane rays, fired at the center of the upper surface. Due to the symmetry of the velocity model, only rays traced in one vertical slice are displayed. The rays bend, and multi-pathing occurs at the lower part of the model. The color represents the traveltime along the rays. Notice that, for equal travel times, the rays traveling outside the lens penetrate deeper than the rays that pass through the lens; the velocity in the lens is lower than in the surrounding medium, leading to longer traveltimes at comparable depths.

Three kinds of caustics are observed in this example. The most visible caustic is the inverted cusped structure just below 2 km. In the neighborhood of the cusp, itself, there are rays from each side of central axis that are approaching the caustic curve, but have not reached it yet and there are rays that have already impinged on the caustic and moved on. As one moves out along the flank of the caustic, below it, there are only two nearby caustic rays, one that has not yet passed through the caustic and the other which has. We emphasize these caustic rays because ray theoretic models that characterize the wavefield here require representations in terms of Airy functions and their generalizations. In this development, we only model the wavefield before and after the caustic and not in the caustic transition zone. Thus there is the cusp of the caustic—the minimum depth of crossing rays—and the smooth flank of the cusped surface. This accounts for two caustics.

The third caustic is less apparent in this figure because it requires 3D visualization for clearer depiction. However, it can still be described in this figure. Below the cusped surface, we see rays crossing on the center vertical line. In 3D, these are two rays of an entire sheet of rays of a surface of revolution. This is the third type of caustic. That is rays with the same polar take-off angle

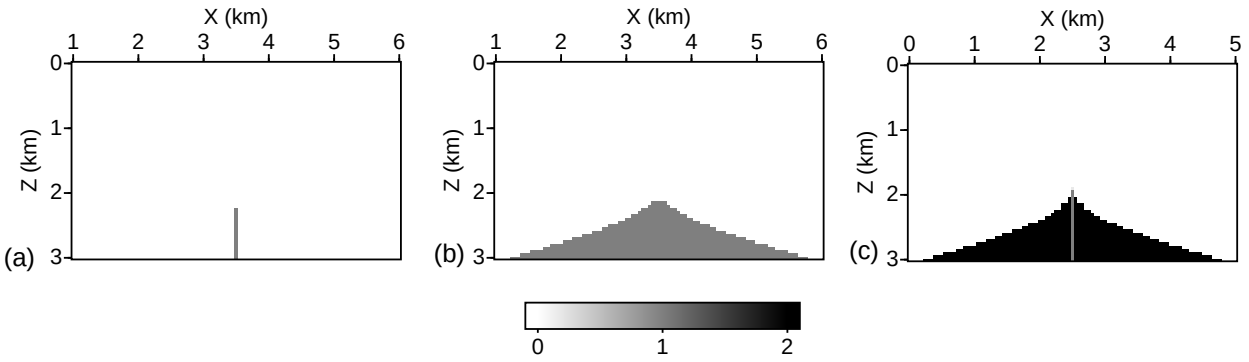

Figure 9. Phase shifts of (a)first arrivals; (b)second arrivals; (c)third arrivals.

and varying azimuthal take-off angle form a caustic on the axis. Varying the polar angle moves the caustic point along the axis.

For each of these caustics, the Jacobian used in amplitude calculations vanishes. Thus, the Jacobian matrix has at least one zero eigenvalue and corresponding eigen vector that characterize the direction in which the cross-sectional area of a ray tube has shrunk to zero. At the cusp, two eigenvalues vanish, corresponding to variations with respect to the two initial take-off angles. Along the flank of the cusp, the principle direction of vanishing corresponds to the vanishing of the Jacobian with respect to variations in the polar angle, while at the on-axis caustic below the cusp, the vanishing is with respect to variations in the azimuthal angle.

Figure 6 shows the first arrival traveltime. In the triplication region, the shapes of the wavefronts are those generated by connecting the ray endpoints that have been traced from outside the lens. The pull-up of the wavefronts under the lens is due to the low velocity in the lens.

Figure 7 shows the amplitude of first arrivals. The amplitudes shown in this plot are consistent with the ray coverage in Fig 5. The high intensity of amplitude in the region of the cusp characterizes the relative increase in the density of rays. The WKBJ wavefield modeling is not accurate near caustics where the computed amplitude approaches infinity. The code sets a threshold above which the amplitude is replaced by an upper bound to stabilize the code. The difference shown in the amplitude between first and second order caustics is caused by the averaging of the ray amplitude inside a ray tube of prescribed size. The actual caustic surfaces form a set of measure zero in 3D. Thus, we anticipate that this approximation in caustic regions will not seriously effect the amplitude of the output, except perhaps, at image points that are also caustic points of the ray fields for the Green's functions from source and receiver. In fact, the entire theory employed for inversion breaks down in the neighborhood of such points and even the imaging produced by migration alone is somewhat suspect.

Figure 8 shows the amplitude of most energetic arrivals. Figures 7 and 8 show the same amplitudes in the upper part of the figure, including the region on axis directly below the source point. These are regions in which the first arrival *is* the most energetic arrival. On the other hand, the amplitudes are quite different in the triplication region below the cusped caustic. The amplitudes of the most energetic arrivals in this region are formed by those rays that have traveled through the lens. As noted in the ray plot, Fig 5, these rays are slower. Hence, the first arrivals and the most energetic arrivals are predictably different here. The difference in position between the first arrival and the most energetic arrival can be 1 km or more.

Figure 9 shows the phase shifts in the triplication region, the area surrounded by the cusp surface. The first arrivals reach the receiver grid points from outside the lens (see Fig 5). Therefore, no phase shifts arise along the ray until the rays approach the axis, on which rays with the same polar take-off angle and varying azimuthal take-off angle form a caustic with phase shift of $\pi/2$. The second arrivals in time also come from rays outside the lens, but from the opposite side of lens with respect to the center axis. As a result, the second arrivals get a phase shift of $\pi/2$ on the axis and carry it further on to all the grid points in the triplication zone (Fig 9b). The third arrivals, the latest arrivals in time, pass through the axis right near the cusp. At the cusp, itself, two eigenvalues vanish. The nearby rays first pass through the caustic on the axis corresponding the vanishing of the eigenvalue with eigenvector in the direction of azimuthal angle. The rays then pass through the caustic along the flanks leading out from the caustic. Here, the eigenvalue

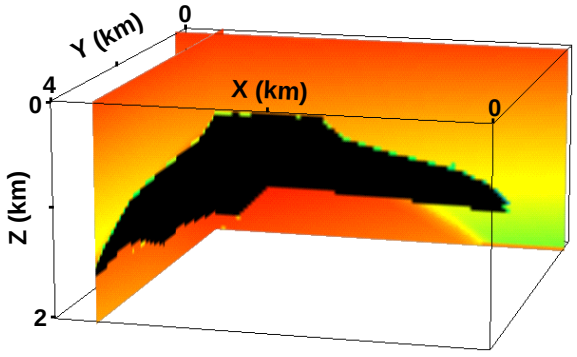

Figure 10. SEG/EAGE salt model. The velocity in the salt(black) is about 4482 m/s.

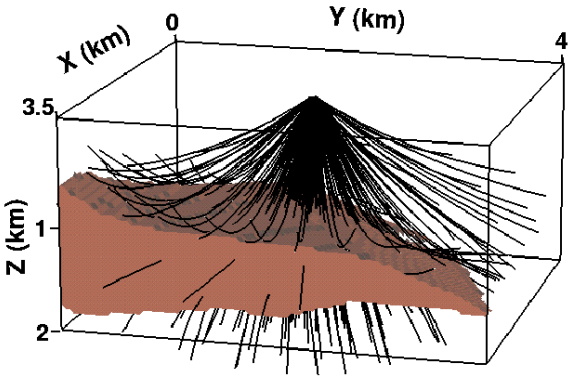

Figure 12. Rays in the salt model.

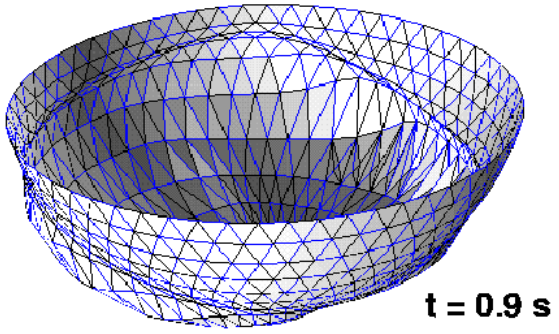

Figure 11. One wavefront recorded at 0.9 s, with the source located at the center of the upper surface.

associated with the polar angle vanishes. The code is able to detect the two sign changes in the Jacobian, and results in a phase shift of π at each grid points (Fig 9c), except that the ray penetrating vertically has no shift; the program computes a phase shift of $\pi/2$ at grid points below the source. However, modeling of on-axis propagation is highly suspect. The cusp is formed by a limit of rays with polar angle approaching zero. Yet, that limiting ray is associated with a limit of axis-crossings by rays forming the caustic flanks below and to the right and left. Thus the limiting ray, which would seem to have initial polar angle equal to zero crosses the axis only once—at the cusp—while the ray with initial polar angle zero remains on-axis throughout its propagation path.

Example III — SEG/EAGE model

The last example uses a section of the SEG/EAGE salt-dome model, which is based on a typical US Gulf Coast salt structure. The complexity of the 3D salt structure makes it a benchmark model used to evaluate various 3D forward modeling and imaging algorithms. Figure 10 shows two slices of the velocity distribution. The velocity in the salt is about 4482 m/s, shown in black. It is much higher than the velocities in the surrounding sediments. As a consequence, the salt body acts as a large secondary source that emanates waves from its surface, nearly in all directions. Such waves, typically, have low energy; however, due to their speed through the salt, they generate first arrivals at near-salt and sub-salt regions. These waves dominate the solution of first arrival eikonal solvers. Some of these waves correspond to head-waves; others are just low-energy forward propagating parts of solutions. Using such a traveltime solution for imaging will result in a less than ideal image. (Geoltrain & Brac, 1993)

Figure 11 is one wavefront recorded at 0.9 s with the source located at the center of the upper surface. Its lower part changes from the typical spherical shape, due to the presence of the high velocity salt. This structure causes portions of the wavefront to bulge and expand, especially those parts that have penetrated through the salt. The boundaries of this bulge are dominated by the pseudo-head-wave arrivals, which continuously connect the portions of the wavefront that penetrated through the salt with those that traveled only through the sediments. However, headwaves are low-energy arrivals that are not useful for imaging applications. Waves traveling directly from the source, without going through the salt, carry more energy than rays that propagate through the salt.

Figure 12 is a ray plot, fired at the center of the upper surface. The front face of this figure shows a vertical slice at x = 3.5km, which is 1.5km from the source. It passes through the salt structure. Rays are also shown in this plot, shot off with a uniform distribution of take-off angles. The feature of adding rays to maintain ray density was suppressed in this figure, so that we could see the relative distribution of the set of rays around the salt

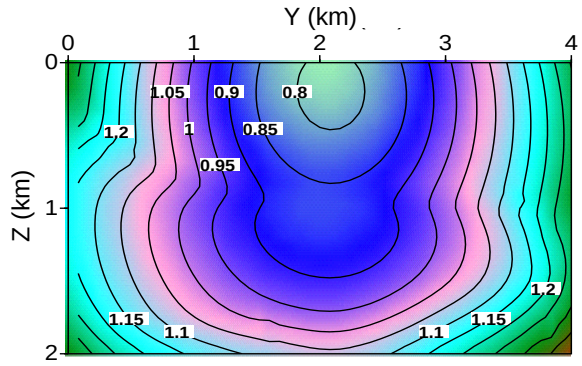

Figure 13. Traveltime at x=3.5 km.

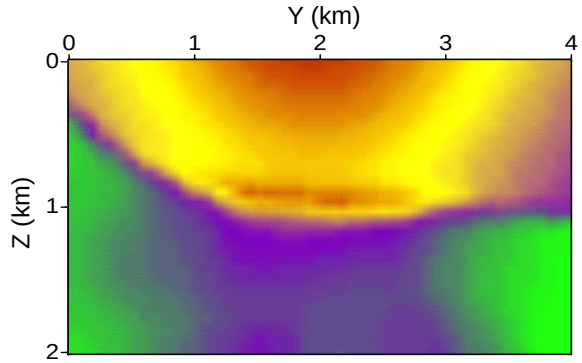

Figure 14. Amplitude at x=3.5 km.

structure, which are initially uniform in take-off angles. Notice that the density of the post-critical rays that do not enter the salt is much higher than that of the rays that enter the salt and emerge through the front face. This indicates that we should expect the amplitude in the salt to be lower than the amplitude right above the salt. Figure 14 is an amplitude plot on the same vertical slice as the front face of Fig 12. Here, the red and yellow colors indicate high amplitude and the purple color, low amplitude. The high and low amplitude zones agree with what we expected from the ray plot in Fig 12. We know from the previous discontinuous example that the amplitudes near turning are not as accurate as the transmitted amplitudes, but they are close enough qualitatively to confirm the agreement we see between these two figures. Figure 13 is the traveltime at the same cross section. The rapid changes of the wavefronts agree with the high velocity of salt.

Conclusions

We have demonstrated the implementation of a ray-theoretical forward modeling algorithm on three progressively more complex earth models. This method is based on dynamic ray tracing and wavefront construction in smoothed gridded earth models. The program efficiently finds all the possible arrivals. The use of smoothing applied to the discontinuous model stabilizes the ray tracing while maintaining sufficient accuracy on transmitted traveltime and amplitude coefficients, excluding transmission coefficients. Re-introduction of transmission coefficients is a topic of ongoing research at this time. The method is capable of calculating all typical ray-tracing parameters such as traveltime, ray amplitude, slowness vector, etc. It can produce all the quantities involved in Bleistein-Cohen inversion formula. The adaptability of the method was demonstrated by evaluating the wavefield in regions of extreme geometrical spreading, such as near a salt wall, in sub-salt regions, and in presence of low velocity lens.

Acknowledgments

The authors wish to acknowledge the support for this project given by the Office of Naval Research, Ocean Acoustics, grant number N00014-95-1-0508. Partial support was also provided by the Sponsors of the Consortium at the Center for Wave Phenomena, Colorado School of Mines.

References

Albertin, U., Cabrera, J., Chang, W., Fouler, P., Stankovic, G., & Ward, L. 1996. A comparison of Kirchhoff migration results for the SEG/EAGE salt model using several traveltime generators. *66th Annual Internat. Mtg., Soc. Expl. Geophys., Expanded Abstracts*, **66**, 562–565.

Audebert, F., Nichols, D., Rekdal, T., Biondi, B., Lumley, D., & Urdaneta, H. 1997. Imaging complex geologic structure with single-arrival Kirchhoff prestack depth migration. *Geophysics*, **62**, 1533–1543.

Bleistein, N., Cohen, J.K., & Hagin, F.G. 1987. Two and one-half dimensional born inversion with an arbitrary reference. *Geophysics*, **52**(1), 26–36.

Bleistein, N., Cohen, J. K., & Stockwell, Jr., J. W. 1996. *Mathematics of Multidimensional Seismic Inversion*. Colorado School of Mines.

Červený, Vlastislav, & de Castro, Mirian A. 1993. Application of dynamic ray tracing in the 3-D inversion

of seismic-reflection data. *Geophys. J. Int.*, **113**, 776–779.

de Hoop, M. V., & Brandsberg-Dahl, S. 1998. Maslov asymptotic extension of Generalized Radon Transform inversion in anisotropic elastic media: a Least-Squares approach. *submitted to Inverse Problem.*

Geoltrain, S., & Brac, J. 1993. Can we image complex structure with first-arrival traveltime. *Geophysics*, **58**, 564–575.

Meng, Z., & Bleistein, N. 1997. Wavefront contruction (WF) ray tracing in tetrahedral models – application to 3-D traveltime and ray path computations. *67th Annual Internat. Mtg., Soc. Expl. Geophys., Expanded Abstracts*, **67**, 1734–1737.

Wang, L., & Bleistein, N. 1998. $3D$ Multivalued Traveltime and Amplitude Maps. *68th Annual Internat. Mtg., Soc. Expl. Geophys., Expanded Abstracts*, **68**, 1879–1882.